

# Design of Conical Corrugated Feed Horns for Wide-Band High-Frequency Applications

Xiaolei Zhang, *Student Member, IEEE*

**Abstract**—This paper presents a new analytical procedure for the design of the conical corrugated feed horns used in the millimeter and submillimeter wavelength range, which could achieve wide-band single-mode operation and wide-band, low return-loss impedance matching simultaneously. A test model of the feed horn designed using this procedure displayed excellent performance, and agreed well with the theoretical predictions [1].

## I. INTRODUCTION

THE wide-band design of a corrugated feed horn requires the simultaneous achievement of wide-band single-mode operation and wide-band, low return-loss impedance matching. So far, no analytical procedure was available in the literature to realize the two goals in the same design. The early analysis of Dragone [7], [8] on feed horn modal fields near cutoff produced a design which optimized the single-mode bandwidth. Unfortunately, the return loss of this design over the entire single-mode bandwidth was not always small. Similar return-losses were also present in many of the other wide-band designs. In recent decades, computer simulations of feed horn performances have been made through calculating the scattering matrix of a series of cascaded cylindrical sections, which made up the grooves and ridges of the horns [2]. These simulations allow certain low return-loss mode launchers to be designed through trial and error on the computers. The numerical design approach requires the availability of the simulation software, and the result is often not optimum in terms of the widest possible bandwidth.

In this paper, a new procedure is presented for the mode-launching region of the corrugated feed horns, which allow the simultaneous achievement of wide-band single-mode operation and wide-band, low return-loss impedance matching over a fractional bandwidth of more than 50%. The procedure is entirely analytical and does not require the availability of simulation programs. In particular, the single-mode and impedance-matching requirements can be dealt with separately, and then combined into one design. The analysis for the single-mode region is very similar to that presented in Dragone [7], [8], although the applicability of his original cutoff conditions are rejustified in the present configurations for the low return-loss design, and several mistakes in his original mode diagram were corrected. The low return loss

part of the design procedure is arrived at through analyzing the results of the space harmonics calculations [5] for feed horns with small aperture sizes, which is appropriate for horns at their throat or mode-launching region. The resulting of the design is also simple to manufacture and avoided the complications of using ring-loaded slots for reducing return loss [3].

For horns used in the millimeter and submillimeter range, the possible choices of the design parameters are limited by the fabrication and cost constraints. The limiting behavior of the feed horns, as we vary the groove coarseness and conical flare angles, are also investigated in this work through computer simulations. The results of these investigations can be used as guidelines for various high-frequency designs.

A model of the corrugated feed horn for the frequency range of 70–115 GHz, designed according to the above principles, has been fabricated and tested [1]. It displayed excellent performance in terms of wide-band single-mode operation and wide-band impedance matching. The measured radiation patterns agree well with the theoretical calculations. Feeds of this type are currently used on the radio telescopes of the Berkeley-Illinois-Maryland Association (BIMA) Interferometer. Together with a tertiary optical train [4], aperture efficiencies of more than 70% are achieved through most of the 70–115 GHz bandwidth. Several submillimeter horns of similar design have also been made.

In what follows, we will first (in Section II) discuss the principles of a conical corrugated feed horn simple terms. We will present the analysis of the fields and modes under the corrugated waveguide boundary conditions in Section III. Section IV gives the details of the new analytical approach for the design of the mode-launching region, which allows the simultaneous achievement of single-mode operation and low return-loss impedance matching over a fractional bandwidth of more than 50%. Comparison of the results of this design to that of other design approached are also given. Then in Section V we present the result of numerical simulation which could be used as guidelines for the determination of groove dimensions and horn flare angle, especially for high-frequency applications. Section VI gives an example of the design, which was used as a test model to verify the new design approach. Some of the measurement results, the comparison to the theoretical predictions, and an outline of the BIMA optical train which integrates this feed horn and two dielectric lenses are also given. Section VII is the concluding section which summarizes the main results obtain in this work. The Appendix contains the design procedure for the rectangular-

Manuscript received May 26, 1992; revised October 5, 1992.

The author was with the Radio Astronomy Laboratory and the Department of Electrical Engineering and Computer Science, University of California, Berkeley, CA. She is now with the Harvard-Smithsonian Center for Astrophysics, Cambridge, MA 02138.

IEEE Log Number 9208366.

to-circular waveguide transition section. A similar transition section is manufactured as an integral part of the feed horn in the test model.

## II. PRINCIPLES OF CONICAL CORRUGATED FEED HORNS

The idea and prototypes of the corrugated feed horns were originated in the early 1960's to achieve low sidelobe and symmetric beam radiation patterns. Diffraction analysis has shown that most of the backlobe structure of a pyramidal horn results from energy diffracted by the E-plane edges. This can be understood by the well-known fact that the far-field pattern of a horn antenna is the Fourier transform of its aperture field distribution. The discontinuity of the step distribution at the E-plane edge of a pyramidal horn is responsible for the higher sidelobe levels in its far field. The E- and H-plane radiation patterns of the pyramidal horns are also nonsymmetric.

On the other hand, the single (dominant)-mode corrugated feed horn has mainly a  $J_0(\kappa r)\hat{x}$  distribution over the aperture, with the first zero of  $J_0$  falling on the edge of the aperture. This distribution has a much smoother truncation near the edge of the aperture and thus a much lower sidelobe level in the far-field patterns. It also offers a nearly perfect circularly symmetric and linearly polarized beam. By doing mode synthesis using many HE-type feed horn modes, an even smoother aperture distribution and even lower sidelobe levels in the far field can be achieved.

Although a complete understanding of the feed horn working principles involves the solution of Maxwell's equations under the boundary condition of the feed horn corrugations (the details of which will be described in the later sections), the main result of this solution is easy to understand. A small flare-angled corrugated feed horn can be approximated by a corrugated waveguide of constant cross section, with the effect of the horn flare angle being taken into account by superposing a spherical cap phase distribution to the aperture field solution. In corrugated waveguide of large enough diameter, two sets of modes can propagate. These are termed  $HE_{1n}$  and  $EH_{1n}$  modes. ( $n$  is the number of the roots of either the first-order Bessel function  $J_1$ , or the number of roots of  $J_1$ 's first derivative. These roots appear in the expressions of the  $HE_{11}$  and  $EH_{11}$  fields, respectively.) Here  $EH_{1n}$  modes are usually undesirable, since they cause beam asymmetry and crosspolarized radiations. The  $HE_{1n}$  modes, on the other hand, can all be used, at least in principle, to do pattern synthesis. In practice, due to mode phase slippage inside the horn, multimode horns are basically excluded from the wide-band designs. Single-mode horns usually have a sidelobe level of about -25 dB, which is good enough for most applications.

In the design of the corrugated feed horns, the so-called "throat" or mode-launching region is the most crucial and difficult part. Since, when the horn starts to flare to bigger apertures, the size of the horn will allow almost all of the  $HE_{1n}$  and  $EH_{1n}$  modes to propagate, we can only select the desirable modes in the throat region, where the horn dimension is still small enough to allow the cutoff of the unwanted modes. Besides acting as the mode launcher and selector, the throat region should also be an impedance transformer,

achieving the smooth conversion of the circular waveguide  $TE_{11}$  mode to the corrugated waveguide  $HE_{11}$  mode. The impedance matching and mode selecting function should work over the entire bandwidth of interests. In the current design of the feed horn, carefully chosen parameters for the throat region allow almost all of the above-mentioned goals to be achieved.

The design for the main body of the feed horn concerns flaring the throat region to the correct size with the proper flare angle, in order to satisfy the requirements placed by the system optics. The groove dimensions of the horn also have to be carefully chosen such that mode conversion inside the horn body is small.

In the following sections, more rigorous analyses and calculations for the corrugated feed horn design are given.

## III. FIELDS IN THE CORRUGATED WAVEGUIDE

In general, the modes inside a corrugated waveguide can be written as the superposition of the circular waveguide TE and TM modes of corresponding order traveling at the same longitudinal velocity. In a metallic wall circular waveguide of fixed radius, the TE and TM modes will in general have different phase velocities in the propagation direction, owing to their distinct transverse wave velocities, required by the boundary conditions for the TE and TM cases. In order to equalize the transverse (and thus longitudinal) wave velocities, the TE and TM waves should effectively see different boundary conditions or surface impedances. This type of "anisotropic" boundary condition can be realized by azimuthally grooving the metallic wall, resulting in the so-called "corrugated waveguide." In what follows, we will briefly summarize the solutions of corrugated waveguide fields [5]–[8].

Assuming  $\cos \Phi$  azimuthal variations, the fields inside a corrugated waveguide ( $r \leq a$ ) can be written as a superposition of a circular waveguide  $TE_1$  and  $TM_1$  modes (Fig. 1):

$$\begin{aligned} E_z &= A J_1(\kappa r) \cos \Phi e^{-j\beta z} \\ H_z &= \frac{1}{Z_0} B J_1(\kappa r) \sin \Phi e^{-j\beta z} \\ E_\Phi &= \frac{j}{\sin \theta_1} \left[ B J_1'(\kappa r) + A \cos \theta_1 \frac{J_1(\kappa r)}{\kappa r} \right] \sin \Phi e^{-j\beta z} \\ H_\Phi &= \frac{1}{Z_0 \sin \theta_1} \left[ A J_1'(\kappa r) + B \cos \theta_1 \frac{J_1(\kappa r)}{\kappa r} \right] \cos \Phi e^{-j\beta z} \\ E_\rho &= \frac{-j}{\sin \theta_1} \left[ B \frac{J_1(\kappa r)}{\kappa r} + A \cos \theta_1 J_1'(\kappa r) \right] \cos \Phi e^{-j\beta z} \\ H_\rho &= \frac{-j}{\sin \theta_1} \left[ A \frac{J_1(\kappa r)}{\kappa r} + B \cos \theta_1 J_1'(\kappa r) \right] \sin \Phi e^{-j\beta z} \quad (1) \end{aligned}$$

where

$$\begin{aligned} \kappa &= k \sin \theta_1 \\ \beta &= k \cos \theta_1 \\ \kappa^2 + \beta^2 &= k^2 \quad (2) \end{aligned}$$

and  $Z_0$  is the free space wave impedance.

When the aperture size of the waveguide is large compared to wavelength (whereas the small aperture effects will be considered in the next section), higher space harmonics with

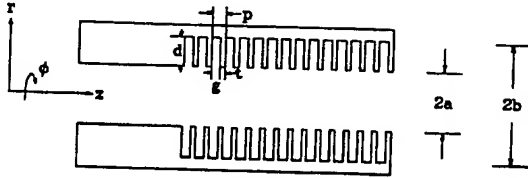


Fig. 1. Corrugated waveguide.

$\beta = \beta_0 + 2\pi N/p$  (where  $N > 1$  and  $p$  is the pitch of the grooves) can be ignored, i.e., we assume that  $\beta$  is a constant. When there are also enough grooves per wavelength, the so-called "surface impedance" approximation can be used. In this approximation, we assume that the effect of the corrugation can be approximated by an equivalent (anisotropic) surface impedance. In obtaining this surface impedance, we also assume that there are only TM ( $E_z, H_\phi, H_r$ )-type standing waves inside the slots and no TE-type standing waves. The boundary conditions become

$$E_\phi = 0 \quad (3a)$$

$$\frac{H_\phi}{E_z} = -\frac{1}{jX_s} \quad \text{at } r = a \quad (3b)$$

where

$$jX_s = jZ_0 \tan(kd) \left(1 - \frac{t}{p}\right) \quad (3c)$$

and the meanings of  $t, p$ , and  $d$  can be found from Fig. 1.

Substitute the expressions for the fields (1) into the above boundary conditions; (3) becomes

$$\gamma \equiv \frac{A}{B} = -\frac{u}{\cos \theta_1} \frac{J'_1(u)}{J_1(u)} \quad (4a)$$

$$y \equiv -\frac{Z_0}{X_s} = \frac{\cos \theta_1}{\sin \theta_1} \frac{1}{\gamma} + \frac{1}{\sin \theta_1} \frac{J'_1(u)}{J_1(u)} \quad (4b)$$

where  $u \equiv ka \sin \theta_1 = \kappa a$ .

Eliminating  $\gamma$  from the above two equations, we get

$$\frac{y}{ka} = \frac{1}{u^2} \frac{J_1(u)}{J'_1(u)} \left[ \left( \frac{u J'_1(u)}{J_1(u)} \right)^2 - 1 + \frac{u^2}{(ka)^2} \right]. \quad (5)$$

For  $ka \gg 1$ ,  $\theta_1 \approx 0$ , and for  $u, y$  finite, this expression reduces to

$$\left( \frac{J'_1(u)}{J_1(u)} u \right)^2 - 1 = 0. \quad (6)$$

The two roots of the above equation are

$$\frac{J'_1(u)u}{J_1(u)} = -1, \quad \text{or } \gamma = 1 \text{ or } J_0(u) = 0 \quad (7a)$$

$$\frac{J'_1(u)u}{J_1(u)} = 1, \quad \text{or } \gamma = -1 \text{ or } J_2(u) = 0. \quad (7b)$$

Here the condition  $\gamma = \pm 1$  is called the "balanced hybrid" condition, which corresponds to an equal amplitude, in (or out of) phase superposition of TE and TM modes.

Therefore, for large  $ka$ , two sets of modes can exist inside the corrugated waveguide, corresponding to the solutions of

the above two boundary equations

$$\text{HE}_{1n} \text{ modes, } u = u_{0n} \quad (n = 1, 2, 3, \dots), \text{ roots of } J_0 \quad (8a)$$

$$\text{EH}_{1n} \text{ modes, } u = u_{2n} \quad (n = 1, 2, 3, \dots), \text{ roots of } J_2. \quad (8b)$$

Using the balanced hybrid condition, we can thus write the transverse components of the fields in the corrugated waveguide as

HE<sub>1n</sub> modes

$$\vec{E}_t = -j \frac{ka}{u} A \left[ J_0\left(\frac{r}{a}u\right) \vec{i}_x + \frac{1}{4} u^2 \frac{y}{ka} J_2\left(\frac{r}{a}u\right) \cdot (\cos 2\Phi \vec{i}_x + \sin 2\Phi \vec{i}_y) \right] e^{-j\beta z} \quad (9a)$$

$(u = u_{0n})$

EH<sub>1n</sub> modes

$$\vec{E}_t = j \frac{ka}{u} A \left[ J_2\left(\frac{r}{a}u\right) (\cos 2\Phi \vec{i}_x + \sin 2\Phi \vec{i}_y) \right] e^{-j\beta z} \quad (9b)$$

$(u = u_{2n})$

What we would like for the aperture field of the feed horn is a smooth radial distribution, including a smooth taper at the edge of the aperture, a symmetric azimuthal distribution, and a single linearly polarized direction for the fields. From the field expressions we obtained for HE and EH modes (9a), (9b), we see that these features can only be achieved by the HE group of modes in the limit of  $y/ka \rightarrow 0$ , and can never be achieved by the EH group of modes.

For the feed horns we normally use, the size of the waveguide near the aperture of the horn is usually big enough to support both types of modes. The only way to avoid the EH type of modes is not to excite them, or to cutoff these modes in the mode-launching region of the horn. As for the modes within the HE group, since the second term in the field expression (9) will introduce beam asymmetry and cross polarization, we need to have either  $y \rightarrow 0$  (which means the depth of the groove  $d \rightarrow \lambda/4$ ) or  $ka \rightarrow \infty$ . In practice, the first condition,  $d \rightarrow \lambda/4$ , is usually satisfied at the center of the operation band by properly choosing the groove depth; and the second condition,  $ka \rightarrow \infty$ , is approximated near the aperture for most of the aperture sizes in practical use.

There is also a more intuitive way to understand the forms of boundary conditions and the solutions of the fields. We know from the basics of the solution of circular waveguides that a TE mode is completely determined by its  $H_z$  component or, more exactly, by the boundary condition that constraints the  $H_z$  component  $\partial H_z / \partial r = 0$ . Duality tells us that for balanced hybrid fields, we would like to have the TM fields to satisfy boundary condition of the dual form  $\partial E_z / \partial r = 0$ .

For the type of boundary conditions provided by the feed horn corrugation, we see that for te field

$$\frac{\partial H_z}{\partial r} \approx E_\phi \approx 0$$

and for TM field

$$\frac{\partial E_z}{\partial r} \approx H_\phi \approx -\frac{E_z}{jX_s}.$$

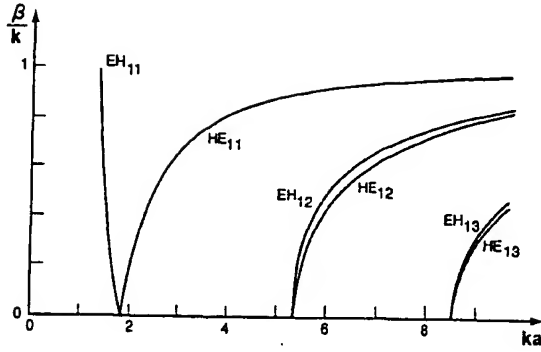


Fig. 2. Propagation diagram for corrugated waveguide modes under the balanced hybrid condition ( $y = 0, \gamma = \pm 1$ ).

In order to achieve  $\partial E_z / \partial r = 0$ , we need either  $X_s \rightarrow \infty$ , which means  $d \rightarrow \lambda/4$ , or  $E_z \rightarrow 0$ , which means  $ka \rightarrow \infty$ . These are essentially the same results as we had obtained from the above more rigorous analysis.

The mode propagation (dispersion) diagram can be obtained from (2) and (4b) under the surface impedance approximation and balanced hybrid condition ( $y = 0, \gamma = \pm 1$ ). Upon solving

$$\left(\frac{u}{a}\right)^2 + \beta^2 = k^2$$

and

$$\gamma \beta J_1(u) + J_1'(u) u k = 0$$

where the solutions of  $u$  are close to the roots of  $J_1'(u) = 0$  for both HE and EH modes near cutoff ( $\beta \approx 0$ ), and the solutions for  $u$  are close to the roots of  $J_0(u) = 0$  and  $J_2(u) = 0$  for HE and EH modes, respectively, for  $\beta \approx k$  (which implies  $ka \gg 1$ , except for  $EH_{11}$  mode), we obtain the relation between  $\beta$  and  $k$  as in Fig. 2.

#### IV. DESIGN OF THE MODE LAUNCHING REGION

From Section III we learned that the  $HE_{1n}$  group of modes give the often desired circularly symmetric and linearly polarized beam. Specifically, for wide-band designs, we are interested in generating only the  $HE_{11}$  mode, which has a pure  $J_0(\kappa r)$  distribution over the aperture of the horn, with the first zero of  $J_0$  lying on the boundary. However, for the usual aperture sizes, both the HE and EH types of modes will be supported. The only way to ensure single-mode operation is to design a mode-launching region at the throat of the horn such that all the higher order modes are cut off by the geometry of the throat. The mode-launching region has yet another equally important function, which is to achieve gradual transition from the impedance of a circular waveguide at the beginning of the throat to that of a corrugated waveguide at the end of the throat. All the mode-selection and impedance-matching functions have to be achieved over the entire frequency band of operation.

#### A. Throat Region Design for Single-Mode Operation

Dragone was the first to give a detailed analysis of modal cutoff behavior [8]. By combining the two boundary conditions in (4), we get (without employing the approximation of  $ka \rightarrow \infty$ , since near the cutoff  $ka$  is usually small)

$$\gamma^2 + \gamma\omega - 1 = 0 \quad (10)$$

where

$$\omega = \frac{yu^2}{ka \cos \theta_1} \quad (11)$$

which has the solutions

$$\gamma_1 = \frac{-\omega + \sqrt{\omega^2 + 4}}{2} \quad (12a)$$

$$\gamma_2 = \frac{-\omega - \sqrt{\omega^2 + 4}}{2} \quad (12b)$$

These correspond to HE and EH modes in the limit of  $ka \rightarrow \infty$  ( $\gamma \rightarrow \pm 1$ ), respectively.

The condition for the cutoff of a mode is that its  $z$  direction propagation constant goes to zero, i.e.,  $\beta \rightarrow 0$  and  $\cos \theta_1 = \beta/k \rightarrow 0$ . For  $y \neq 0$ , according to (11), this will give  $|\omega| \rightarrow \infty$ . Therefore, we obtain

$$\gamma_1 \rightarrow \begin{cases} 0 & \text{if } y > 0 \\ \infty & \text{if } y < 0 \end{cases} \quad (13a)$$

$$-\gamma_2 \rightarrow \begin{cases} \infty & \text{if } y > 0 \\ 0 & \text{if } y < 0 \end{cases} \quad (13b)$$

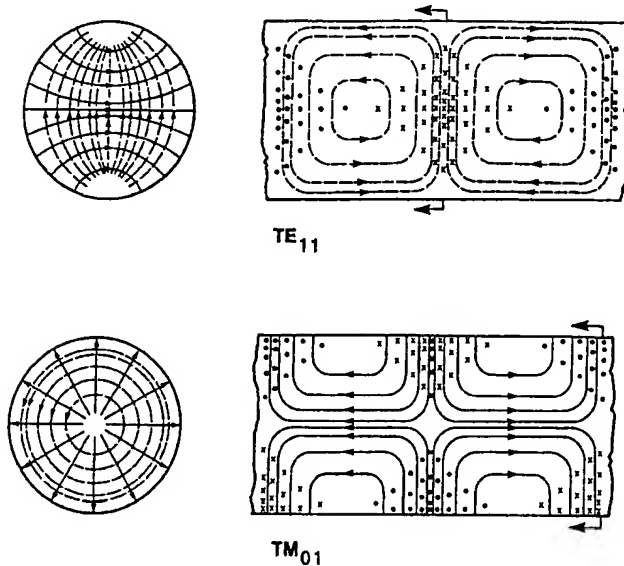
If  $\gamma = 0$ , this is a TE-type cutoff (since  $\gamma$  is defined as the ratio of TM and TE modes). In this case, inside the main waveguide  $H_z \neq 0, E_z = 0$ , thus the surface reactance  $X_s$  has no effect on the cutoff. We can therefore replace the corrugated waveguide with a circular waveguide of radius  $a$ . The condition for the te type of cutoff is thus the same as that for a te mode in a circular waveguide (with  $\kappa \rightarrow k$  as  $\beta \rightarrow 0$ )

$$J_1'(ka) = 0. \quad (14)$$

If  $\gamma \rightarrow \infty$ , the cutoff is TM type. The only nonzero  $z$  component of the field is  $E_z$ . If the disk making up the groove is thin, the fields can penetrate inside the slot region. Therefore, we can replace the corrugated waveguide with a circular waveguide of radius  $b$ . Thus, the condition for the TM type of cutoff becomes

$$J_1(kb) = 0. \quad (15)$$

Later, we will find that the type of design which leads to low return-loss impedance matching usually has fairly wide disks. The natural question to ask is whether the cutoff conditions (14), (15) are still valid in this case. The answer is yes. In fact, whether or not the field can penetrate the slots in the cutoff region can be seen directly from the TE and TM field distributions inside the circular waveguide (Fig. 3). For the TE wave, since the H field (dashed lines) has longitudinal component, the boundary condition will prevent it from penetrating into the slots, we thus have  $r = a$  as the radius of the corresponding waveguide. For the TM case, the magnetic field has no longitudinal component, both the E and


 Fig. 3. Circular waveguide model fields:  $TE_{11}$  and  $TM_{01}$  modes.

$H$  field can penetrate inside the slots in the cutoff situation. Therefore, the corresponding waveguide radius is  $r = b$ .

When  $y = 0$ , from (4b) we get

$$J_1'(ka) = 0 \quad (16)$$

for  $y = 0$  and  $\cos \theta_1 = 0$ ; i.e., in this case, HE and EH modes have the same cutoff. This later point can also be seen from the mode dispersion diagram (Fig. 2).

Besides, when  $y < 0$ , there can also exist a surface type of mode [8] which is again undesirable. In practice, we choose our dimensions in the throat such that we always have  $y > 0$ .

From the above discussions, we get the following mode diagram (Fig. 4). Several mistakes have been corrected compared to the original mode diagram given by Dragone [8]. These include: the region originally marked for "both  $HE_{11}$  and  $EH_{11}$ " propagation is now changed to that for "both  $HE_{11}$  and  $EH_{12}$ " propagation; the labels for  $|y| = \text{constant}$  lines; and, most importantly, in Dragone's original figure the  $y = 0$  line was plotted with the wrong slope and thus had the wrong intersection with the  $ka = 1.841$  line (the current  $y = 0$  line intersects the  $ka = 1.841$  line at  $kb = 3.526$ ). This results in an underestimate of the maximum single-mode range, with the corrected value being 60% instead of the originally estimated 50% [8] (see, however, also the discussions below for the determination of the bandwidth of the throat region).

In a wide-band corrugated feed horn design, usually only the dominant  $HE_{11}$  mode is desired. But, in practice, a small amount of  $EH_{11}$  can be tolerated since, from looking at the mode dispersion diagram in Fig. 2, we see that as  $ka$  increases the  $\beta$  corresponds to  $EH_{11}$  decreases to zero. This means that even if we excited some  $EH_{11}$  mode in the beginning, it will die off as  $ka$  gets slightly larger inside the throat region.

The region for  $HE_{11}$  only propagation (ignoring the  $EH_{11}$  mode) is indicated by the shaded area. The maximum range of single-mode-operation choice corresponds to the part of the short-dashed line inside the shaded region, with the highest frequency point marked  $\omega_1$  and the lowest frequency point

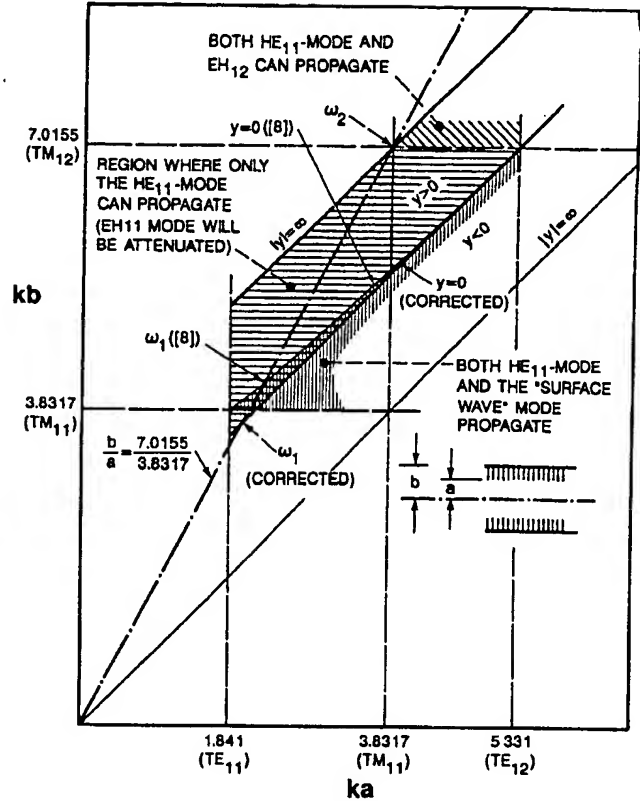


Fig. 4. Mode diagram for corrugated waveguide.

marked  $\omega_2$ . This results in a particular set of values for  $a$  and  $b$  (or more exactly the ratio of the two) near the beginning of the throat. To determine the size of  $a$ , we also need to consider the mode content in the circular waveguide section (see the Appendix for details). This latter consideration will in general give a value not very different from that determined by the maximum-bandwidth consideration alone. After determining the size of  $a$  according to single-mode requirement in the circular waveguide, the corresponding  $b$  is determined by compromising between placing the operation points close to the optimum  $b/a$  line, and placing the highest frequency operation point as close as possible to the boundary of the single-mode region, so as to achieve the maximum bandwidth in a design. This will in general give  $d = b - a \approx \lambda_{0h}/2$ , where  $\lambda_{0h}$  is the free space wavelength at the highest operation frequency. These choices of  $a, b$  at the beginning of the throat generally give a maximum bandwidth of about 60% (after corrections to the results in [8]). Although, considering the fact that we must allow some length of the throat region for the unwanted modes to die out, the actual single-mode bandwidth in either case has to be decreased somewhat (due to the fact that, we have to allow some physical length of the single-mode throat region, usually on the order of one or two wavelengths, to ensure that higher order modes attenuate. On Fig. 4 this corresponds to allowing some length of the single-mode region to the right of the frequency line  $\omega_1, \omega_2$ . Thus, the true single-mode region is somewhat smaller, mainly in the low-frequency end, than what was indicated by the  $\omega_1, \omega_2$  line).

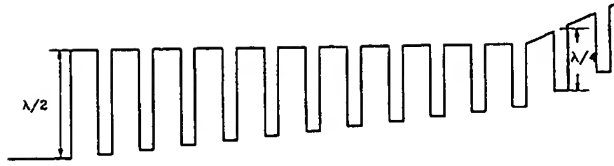


Fig. 5. Possible choice of the throat design for single-mode operation.

The throat then gradually flares the depth of the grooves from  $\lambda_{0h}/2$  to  $\lambda_{0c}/4$  (where  $\lambda_{0c}$  is the free space wavelength at the center of the operation band) over a distance of several wavelengths, to ensure gradual transition of surface impedance and the cutoff of higher order modes. In the current design, this flare of groove depth is realized by changing the parameter  $a$  only, while keeping  $b$  always constant inside the throat. As we move along the throat region, the operation point for different frequencies will move on the mode diagram (Fig. 4) along a series of horizontal lines starting from the points on the line  $\omega_1\omega_2$ . This type of throat design generally gives the widest physical distance of single-mode propagation while we move within the throat region. The schematics for the throat design according to the single-mode requirement alone is shown in Fig. 5.

### B. Impedance-Matching Considerations

The mode-launching region, or the "throat," should act at the same time as an impedance transformer, which gradually transforms the field distribution inside a circular waveguide to that of a corrugated waveguide. This is realized by a smooth transition of the boundary conditions.

The theory of transmission lines tells us that a uniform transmission line of length  $d$  can transform the terminal impedance to the input port in a way such that  $Z_{in} = Z_t \tan kd$ . This tells us that a transmission line of length  $d = \lambda/2$  will exactly reflect the terminal impedance to the input port. This relation suggests that a slot depth of  $\lambda/2$  will effectively create the same surface impedance as the perfect metal wall. It seems that our previous choice of the throat design for single-mode operation (Fig. 5) will fit naturally for the impedance-matching purpose.

Unfortunately this is not usually true. The reasons for this are twofold. First of all, to treat the slots as perfect transmission lines, or to use the impedance transformation relation

$$Z_{in} = jZ_0 \tan kd, \quad (17)$$

where  $Z_0$  is the characteristic impedance of the slot waveguide we have to be in the region  $ka \gg 1$ , and  $kg \ll 1$  (where  $g$  is the width of the groove). When we have only a finite number of grooves per wavelength and are in the region of small  $ka$ , as in the throat, the value of  $d$  used in the impedance transformation formula usually needs to be corrected. Second, the surface impedance on the corrugated surface does not exactly equal  $Z_{in}$  due to the finite thickness of the disks. In the case of sufficient grooves per wavelength, the effect of the disks can

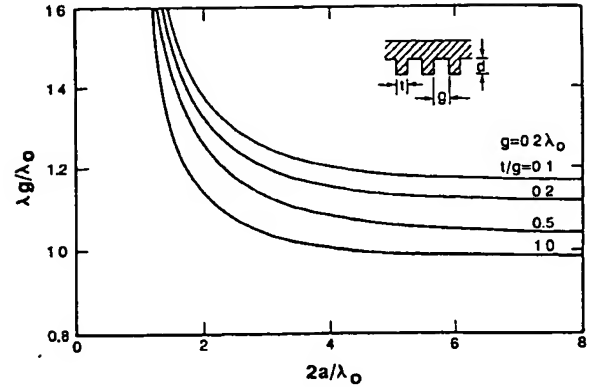


Fig. 6. Effective wavelength in groove waveguide for small aperture corrugated waveguide (revised after Fig. 5.23 of [5]).

be accounted for by introducing an effective surface impedance

$$Z_s = jX_s = Z_{in} \left( 1 - \frac{t}{p} \right) \quad (18)$$

where  $t$  is the thickness of the ridges. From (18) it is clear that when we try to create a resonant groove with  $X_s = \infty$  using a  $\lambda/4$  groove, we will have much less frequency sensitivity if we have small  $t/p$ , i.e., thin ridges compared to groove pitch. This choice of  $t/p$ , as we will show, which is necessary for the grooves of the main horn body, makes the effect of the length correction in the impedance transformation formulas (17), (18) much more prominent in the limit of small  $ka$ . The overall effect of these complications is that a groove depth of  $\lambda_{0h}/2$  at the beginning of the throat will in general fail to give a surface impedance of 0, and in many cases the value of impedance it gives is close to  $\infty$ , as can be seen below.

The effect of small  $ka$ , finite number of grooves per wavelength, and the effect of the ratio of  $t/h$  can be rigorously treated by including all the space harmonics and solving the corrugated waveguide as a periodic structure [5]. One example of the result of this calculation is shown in Fig. 6. Careful observations of this figure show that the guide wavelength in the slots increases for smaller  $ka$  and for small value of  $t/g$ . In the design we will eventually use (Section VI), the choice of initial  $ka$  corresponds to  $2a/\lambda \approx 0.8$ . When we choose to use  $t/g = 1/2$ , with  $g = 0.2\lambda$ , as for the main horn body, the  $\lambda_{0h}/2$  choice of our beginning slot corresponds to roughly  $\lambda_g/4$  in terms of guide wavelength. So instead of achieving  $X_s = 0$ , we actually get  $X_s = \infty$ , which is still the boundary condition of the corrugated wall. This certainly will fail to function as the desired impedance transformer. Further increase in the slot depth will make our other goal of wide-band single-mode operation unattainable.

The way to get around this difficulty comes again from the hint given by Fig. 6. We see that in the case of small  $ka$ , an increase in the value of  $t/g$  (ridge width/groove width) alone will bring the guide wavelength back to the corresponding free space value. This suggests that if we flare both the width and the depth of the groove, i.e., to use longer ( $\lambda_{0h}/2$ ) and thinner ( $t/g = 7$ ) grooves in the beginning of the throat, gradually change it to shorter ( $\lambda_{0c}/4$ ) and wider ( $t/g = 1/2$ ) groove,

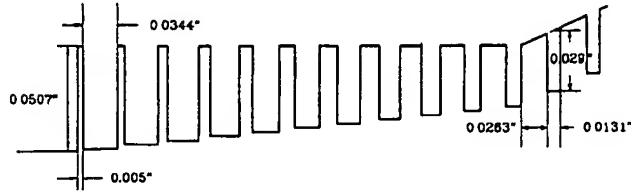


Fig. 7. Throat design for wide-band single-mode and wide-band impedance matching.

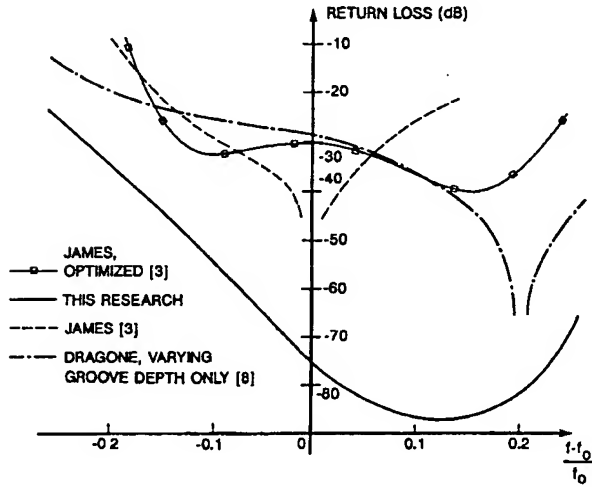


Fig. 8. Calculated return losses of different designs.

we will be able to achieve both the impedance-matching and mode-selection functions. This is exactly what we choose to use in our design of the mode-launching region (Fig. 7). The calculated return-loss characteristics of several mode launchers are compared in Fig. 8. The result for the current design is calculated using a program package CWGSCAT [10], which models the feed horn through cascading the scattering matrices of a series of cylindrical sections which made up the grooves and ridges of the horn. It is obvious that the current design has a much wider frequency bandwidth and lower return loss than the designs using other approaches.

This way of varying both the groove depth and groove width simultaneously to achieve wide-band single-mode operation and wide-band impedance matching, although occasionally being used empirically [9] (since it is natural to make any kind of microwave transition section as smooth as possible), is not present in all the other mode-launcher designs. The reason, the author believes, is that the guide-wavelength variation effect at small  $ka$ , and the necessity of using space harmonics to obtain a rigorous result and to adjust the design parameters correspondingly, have never been fully understood and appreciated by most of the designers. For example, although the effect of groove depth at small  $ka$  was noticed as an increase in the electrical depth of the grooves for small  $ka$  (although not the groove width/ridge width effect), this was not incorporated in Dragone's otherwise fairly rigorous design approach [7], [8]. The most complete corrugated feed horn text of Clarricoats and Olver [5], although included the space harmonics analysis, mainly for the purpose of calculating the

crosspolar radiation characteristics, nonetheless did not make use of this knowledge in the section on mode-launcher design. The lack of either calculations or the detailed measurement results in [9] also prevents the proper evaluation of such a mode launcher.

## V. CHOICE OF THE CONICAL FLARE ANGLE, APERTURE SIZE, AND THE GROOVE DIMENSIONS

After launching the desired  $HE_{11}$  mode in the throat, we would like to design a feed horn flared section with the appropriate outer dimensions and groove sizes such that  $HE_{11}$  mode will propagate to the horn aperture without significant mode conversion into higher order modes. Under single-mode operation, the crosspolar characteristics are determined mainly by the groove dimensions, while the copolar radiation characteristics are controlled by the aperture size and flare angle.

### A. Mode Conversion in a Small Flare-Angled Conical Horn

By assuming  $ka \gg 1$ ,  $y \approx \text{constant}$  and for small flare angled horn, Dragone [7] derived that between two locations along the horn axis  $z = z_1$  and  $z = z_2$ , the converted  $EH_{11}$  mode power  $P_c$  has the following value compared to the incident  $HE_{11}$  power  $P_0$ :

$$P_c = P_0 \times 3.393(10^{-3})y^2 \tan^2 \alpha |1 - e^{j\psi}|^2 \quad (19)$$

where

$$\psi = \frac{10.295}{y \tan \alpha} \frac{y}{ka(z_1)} \left( 1 - \frac{a(z_1)}{a(z_2)} \right) \quad (20)$$

and  $\alpha$  is the flare angle. Therefore,

$$P_c = P_0 \times 1.357(10^{-2})y^2 \tan^2 \alpha. \quad (21)$$

For  $y = 1$ ,

$$\frac{P_c}{P_0} \alpha=4^\circ \approx -42 \text{ dB} \quad (22a)$$

$$\frac{P_c}{P_0} \alpha=16^\circ \approx -29.8 \text{ dB}. \quad (22b)$$

Therefore, if we keep the feed horn flare angle small, and do not operate far from the slot resonance so that  $y$  is not very large, the mode conversion will be small.

### B. Determine the Groove Dimensions for the Crosspolar Radiation Characteristics

We have seen that for a small flare angled horn, the mode conversion along the conical flared section is usually small. The crosspolar radiation characteristics are determined mainly by the intrinsic crosspolarizations of the dominant  $HE_{11}$  mode.

We have derived in Section III that for a corrugated waveguide of radius  $a$ , the electric field due to  $HE_{11}$  mode can be expressed as

$$\vec{E}_t = -j \frac{ka}{u} A \left[ J_0 \left( \frac{r}{a} u \right) \hat{i}_x + \frac{1}{4} u^2 \frac{y}{ka} J_2 \left( \frac{r}{a} u \right) \cdot (\cos 2\Phi \hat{i}_x + \sin 2\Phi \hat{i}_y) \right] e^{-j\beta z}. \quad (23)$$



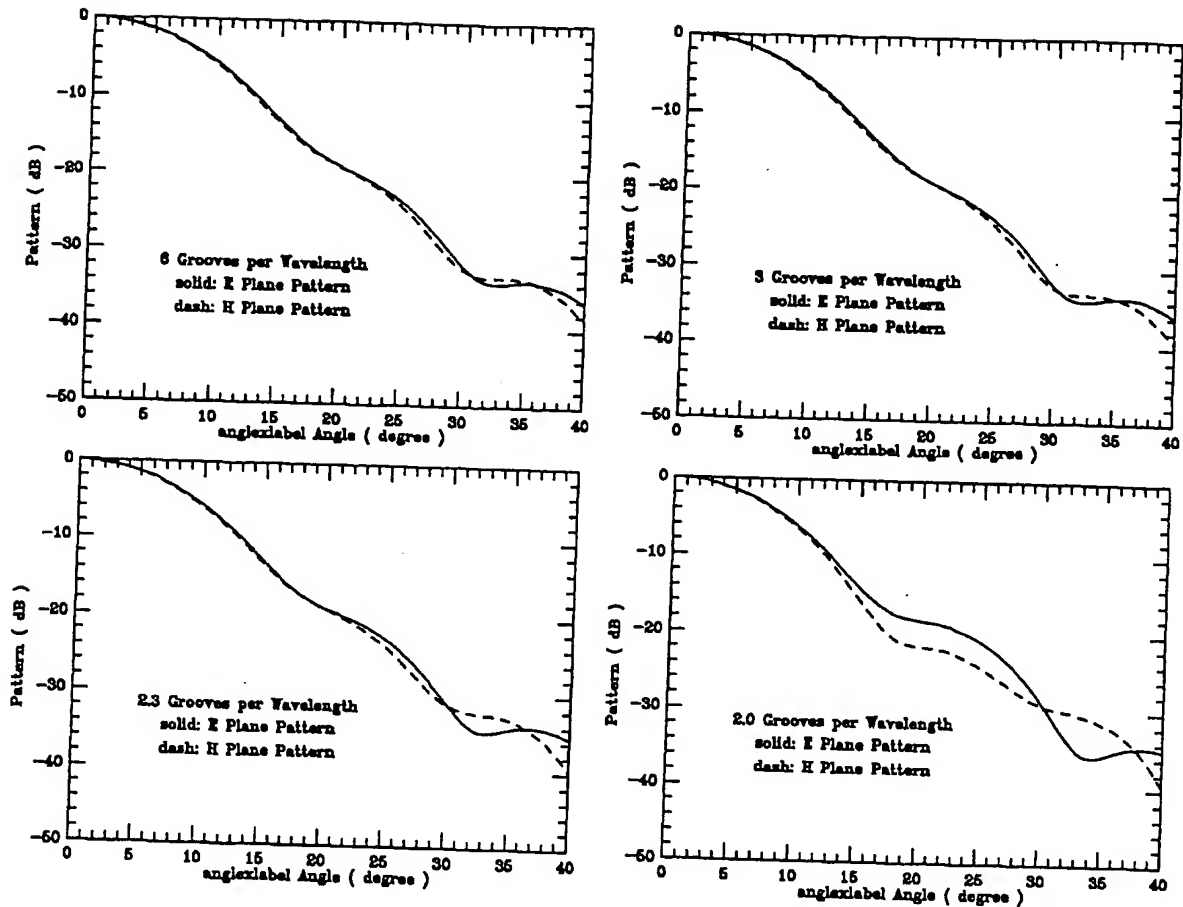


Fig. 9. Groove coarseness tests.

We see from the above field expression that if we want to reduce the value of the second term, which accounts for the beam asymmetry and crosspolar radiations, we can either make  $y = 0$  (grooves at resonance) or  $ka \rightarrow \infty$  (large aperture size).

The aperture size is usually determined by the copolar radiation considerations. For a fixed aperture size, the crosspolar radiation characteristics change with frequency due to the change in surface impedance. Usually the slot depth is chosen such that the resonance occurs near the center of the operation band. The bandwidth characteristics of the crosspolarization levels for different aperture sizes can be found in [5]. For the usual aperture sizes we choose to use, the crosspolarization levels are usually less than -30 to -40 dB.

The groove spacing is chosen such that it satisfies the fabrication and cost constraint, and yet it is fine enough to satisfy the surface impedance approximation. Tests on the groove coarseness effect have been carried out again using the program package CWGSCAT [10]. The results of these tests at 90 GHz are given in Fig. 9. At other selected frequencies, a similar trend is observed. We see that the 3 groove per wavelength results are almost identical to 6 groove per wavelength results, with the slight difference in the E and H plane patterns caused by the intrinsic  $HE_{11}$  radiations (23). As the number of grooves decreases below 3 grooves per wavelength, the E and H plane patterns differ more and more,

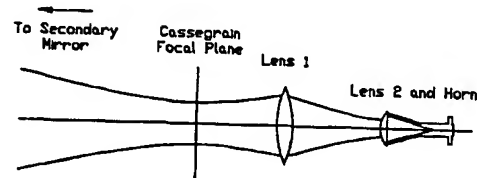


Fig. 10. tertiary optics.

indicating the invasion of higher order modes. It is generally safe in a design if we stay above 2.3 grooves per wavelength at the high end of the operation band. In the current design, we have used a groove dimension which corresponds to 3 grooves per wavelength at the band center and 2.5 grooves per wavelength at the higher frequency end.

### C. Choice of Aperture Size and Horn Flare Angle for Copolar Radiation Characteristics

The radiation patterns of a corrugated feed horn can be determined from the Fourier transform of the aperture field distributions. For feed horns with large enough aperture size and moderate flare angle, the aperture field is mainly of the form of a truncated  $J_0$  amplitude distribution, and a second-order spherical cap phase distribution. The far-field patterns



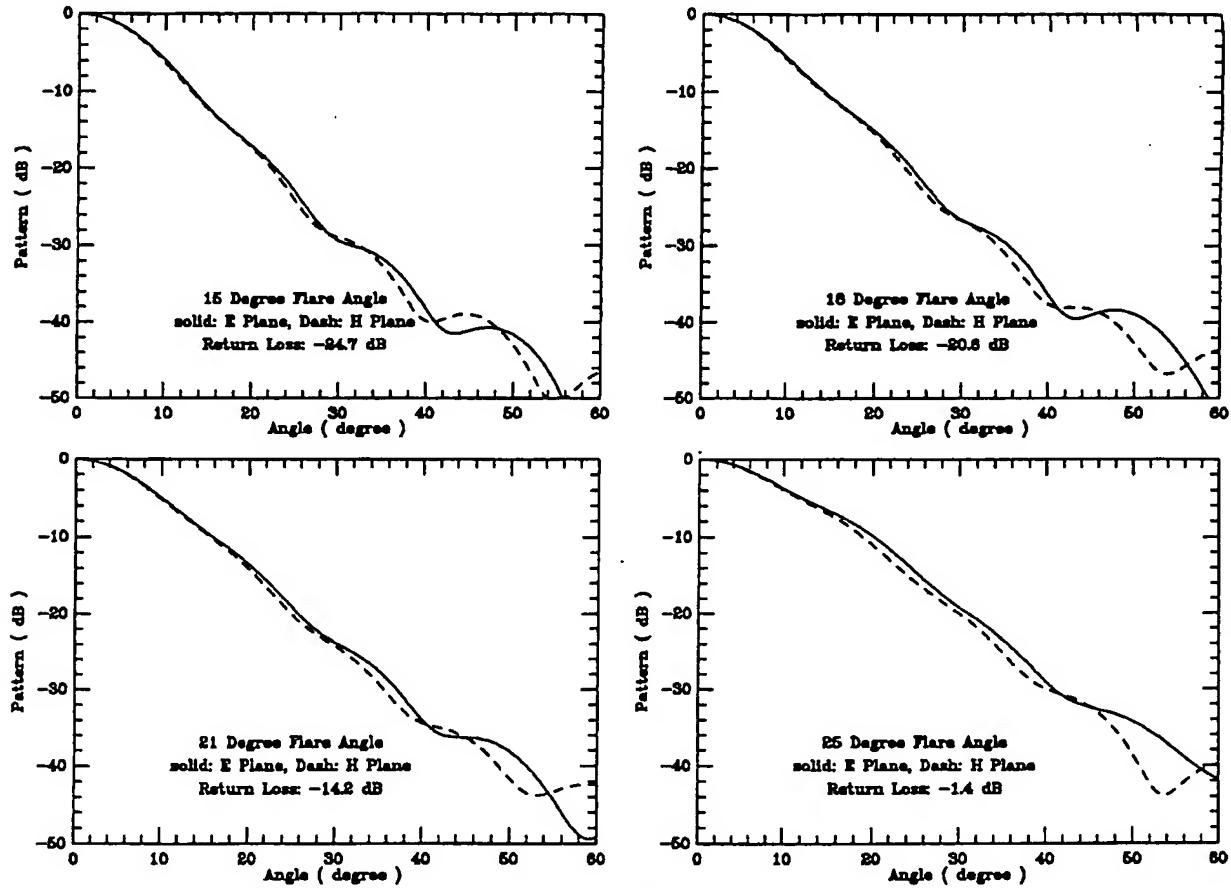


Fig. 11. Flare angle tests.

can be calculated through the Fourier transform of the aperture field.

In the optical train adopted by the BIMA antennas, a tertiary focus optical scheme [4] is used (Fig. 10). Since the beam waist of the telescope field scales with wavelength at the secondary (Cassegrain) focus, while the feed horn field stays the same as frequency changes, if we use another lens to refocus the telescope field to a tertiary focus, we will obtain the image of the telescope aperture, and the size of the beam waist at the position of the tertiary focus is frequency independent. By choosing the proper feed horn aperture size, and the tertiary lens focal length, the match between the telescope field and the feed horn field will also be frequency independent. A phase corrector lens is also used at the aperture of the feed horn to flatten its phase, thus matching the flat wavefront of the incoming telescope field to reduce phase error. This gives a theoretical aperture efficiency (including central 10% radial blockage, or 1% area blockage, of the secondary reflector and including the illumination and spillover losses, but does not include the surface rms loss and feed-leg scattering) of about 84% across the band [4].

The conical flare angle has an added effect of causing reflection at the end of the throat, since there is a discontinuity if the flare angle at the throat and at the horn body are different.

This effect is also tested using the program CWGSCAT, also done at 90 GHz, and the results are summarized in Fig. 11.

## VI. DESIGN PROCEDURE AND THE MEASUREMENT RESULTS

The test model of the new conical horn is intended to cover the 3 mm opacity window of the atmosphere, which has a frequency range 70–115 GHz. The schematics and the parameters for the new conical horn are shown in Figs. 12 and 7. The input surface has the inner cross section of a WR-10 waveguide and it flares gradually into a circular waveguide. The dimension of the WR-10 waveguide has the standard value of 0.05 in by 0.1 in, which can support the rectangular waveguide  $TE_{10}$  mode in the 70–115 GHz range. The procedure to determine the radius of the circular waveguide near the end of the transition section is discussed in the Appendix. The final choice of radius  $a = 0.061$  in allows only the circular waveguide  $TE_{11}$  mode to propagate in the range of 70–118 GHz.

The  $a = 0.061$  in circular waveguide connects to the mode-launching region or "throat" of the feed horn. The throat consists of 11 grooves of varying depth and width, with the pitch of the grooves being uniform and equal to the value used for the main horn body, i.e.,  $p = 0.0394$  in. This value is about 1 groove/mm or 3 grooves/wavelength near 100 GHz. The first groove has a depth of  $d_0 = 0.0507$  in, corresponding to  $\lambda_0/2$

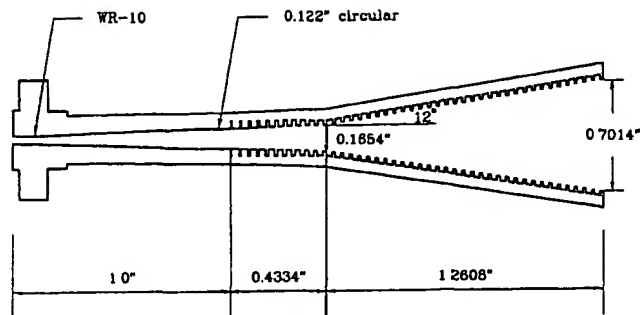


Fig. 12. Design layout for the new conical horn.

near 115 GHz. This choice of initial  $a_0$  and  $b_0 = d_0 + a_0$ , with  $b_0/a_0 = 0.1117/0.061 \approx 7.0155/3.8317$ , corresponds to operation points on the straight line in the mode diagram (Fig. 4), with the 115-GHz point near the top of the intersection of the line with the single-mode region ( $\omega_1$ ) and the 70-GHz point at a little distance above the bottom the intersection of the line with the single-mode region ( $\omega_2$ ), as we vary the frequency. The very large ratio of the initial disk width versus the groove width, i.e.,  $t_0/g_0 = 0.0344/0.005 \approx 7/1$ , makes the value of the guide wavelength inside the slot approximately that of the free space wavelength. This makes it possible for us achieve both the wide-band single-mode operation and wide-band impedance-matching requirements using the same set of throat parameters, as demonstrated in Section IV. The grooves then flare linearly both in depth and width to their values for the main body of the horn at the end of the throat, i.e.,  $t/g = 1/2$ . In the throat region, the  $b$  value or the outer radius at the bottom of the grooves is kept constant till the end of the throat, so that the operation points move horizontally in our mode diagram (Fig. 4) as we move along the throat, keeping the maximum physical distance of single-mode propagation, to ensure that higher order modes have enough distance to decay.

As stated in Section V, the groove dimensions for the main horn body were chosen to achieve the desired crosspolar radiation characteristics. The groove depth  $d = 0.029$  in is chosen so that it is quarter-wavelength at 101 GHz. The choice of the pitch of the grooves  $p = 0.0394$  in corresponds to 3 grooves/wavelength near 100 GHz. The numerical simulations in Section V show that this groove coarseness is enough to ensure  $HE_{11}$  mode propagation without converting it into higher order modes, which happens when the surface impedance approximation breaks down. The ratio of ridge width to groove spacing should be made as small as possible to reduce the frequency sensitivity of the crosspolar radiation characteristics. In practice, this ratio is limited by the electroforming process. As a compromise, a value of  $t/p = 0.33$  or  $t/g = 0.5$  has been used.

The flare angle of the horn has been chosen to be 12 degrees to place it within the category of small flare-angled horn. The conical horn flares to an aperture size of  $a = 0.3507$  in determined by the optics considerations of the new system. This gives a total length of the feed horn (rectangular-to-

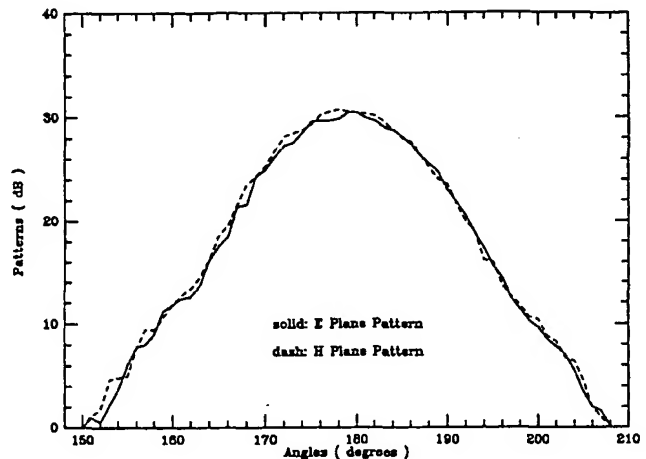


Fig. 13. Measured copolar radiation patterns for the new conical horn.

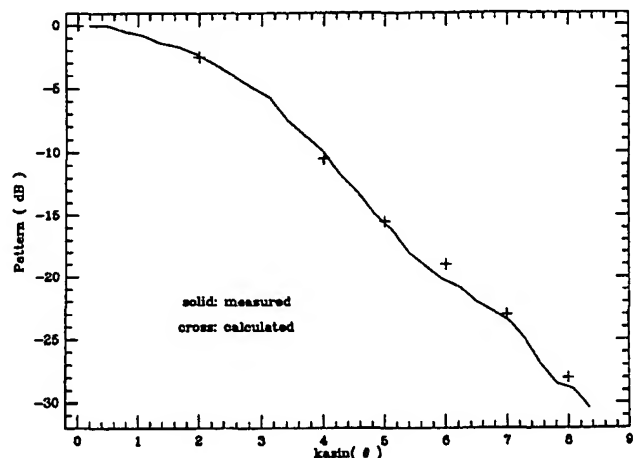


Fig. 14. Comparison between theory and measurement for the copolar radiation patterns.

circular transition section + throat + horn flare) of 2.6942 in. There are 43 grooves altogether.

The design as shown in Figs. 12 and 7 was electroformed by the Custom Microwave Co. in Colorado, and tested at the Radio Astronomy Lab, Berkeley, CA. The results were then compared to the theoretical calculations.

The measured copolar radiation patterns of the new conical horn at 90 GHz is shown in Fig. 13. Pattern symmetry is observed between  $E$  and  $H$  plane patterns, which indicate these are single-mode fields. The copolar patterns are then averaged and plotted in Fig. 14 on a different scale, to ease the comparison to the theoretical results. From this plot, the agreement between theoretical prediction and the measurements is obvious. Similar agreements are also observed at other frequencies all across the

The measured return losses for the new horn are given in Fig. 15. Over most of the frequency range, the return loss is below 30 dB. The oscillations observed on the return-loss plot for the new horn are caused by the internal reflections of the slotted line used for measuring the standing waves. The measured values at the high-frequency end for the new

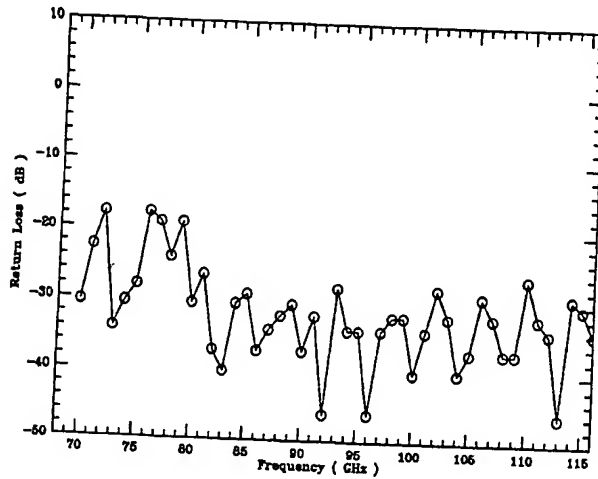


Fig. 15. Measured return losses of the new horn.

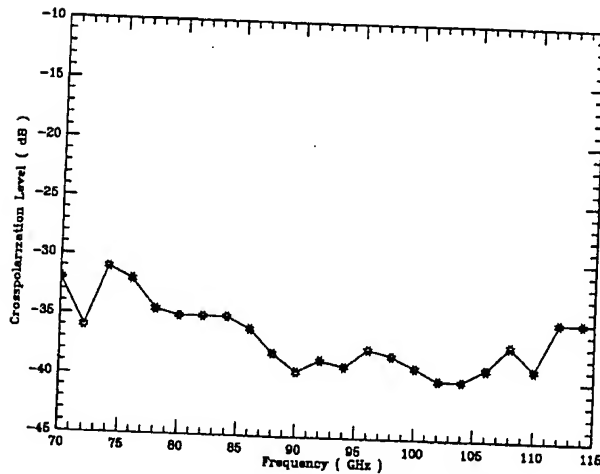


Fig. 16. Measured crosspolarization levels of the new horn.

horn are also limited by the measuring instrument's internal reflections. These instrument-related measurement limitations have been confirmed by performing the same type of return-loss measurement on matched-load terminations. The true values of the return loss of the feed horn for intermediate and high frequencies are expected to be much better than shown on Fig. 16, as the calculations in Fig. 8 indicate.

The measured crosspolarization levels of the new horn are given in Fig. 16. These levels are measured on a plane 45 degrees in between E and H planes, which in general gives maximum values of the crosspolarization. The peak level of the crosspolarization on this plane is searched, and then compared to the copolar peak to get the relative decibel values. The measured crosspolarization results confirmed the single-mode nature of the new horn across the band, and also indicated that the intrinsic  $HE_{11}$  crosspolarization level is low in this design.

This type of corrugated feed horn has been recently installed on the antennas of the Berkeley-Illinois-Maryland millimeter array located at Hat Creek, CA. Aperture efficiency of more than 70% over most of the bandwidth has been measured on one of the antennas with better surface rms. Horns designs, according to the principles stated in this paper, have been

made for frequencies up to 700 GHz, with the mode-launching section containing only five grooves.

## VII. CONCLUSIONS

A new design procedure for conical corrugated feeds is proposed. This design is capable of achieving wide-band single-mode operation and wide-band, low return-loss impedance matching simultaneously. The geometry of the resulting design is simple enough for and low-cost fabrications. Original understandings on the corrugated feed horn working principles and high-frequency limiting behaviors are also obtained. A test model of the feed horn has been carefully measured and has shown excellent performance. The procedure presented in this paper should prove useful to the design of high-performance corrugated feed horns in the millimeter and submillimeter applications.

## APPENDIX

### DESIGN OF THE RECTANGULAR-TO- CIRCULAR WAVEGUIDE TRANSITION SECTION

The mode-launching region (throat) of the feed horn acts as a smooth transition between a corrugated waveguide and a circular waveguide, whereas the standard connection to the mixer block input is a rectangular waveguide. A further rectangular-to-circular waveguide transition section is therefore needed to achieve smooth connection between these two types of waveguides.

The rectangular waveguide used for the 70–115 GHz band is of the type WR-10, which has the cross section dimension  $a = 0.1$  in and  $b = 0.05$  in. For rectangular waveguide  $TE_{mn}$  modes, the cutoff frequency has the following general expression:

$$f_c = \frac{c \sqrt{\left(\frac{m\pi}{a}\right)^2 + \left(\frac{n\pi}{b}\right)^2}}{2\pi} \quad (A1)$$

At any frequency (and the corresponding wavelength), only modes with cutoff frequency smaller (or cutoff wavelength bigger) than the operating frequency (or wavelength) can propagate. Using the dimensions of WR-10 waveguide in this formula, we see that the  $TE_{10}$  mode has a cutoff frequency of 59 GHz, whereas all the other  $TE_{mn}$  modes have cutoff frequencies above 115 GHz. Therefore,  $TE_{10}$  is the only mode that can exist in the WR-10 waveguide in the 70–115 GHz frequency range, which is also the mode we would like to use. The field distributions of rectangular waveguide  $TE_{10}$  mode can be found in any standard microwave text.

The dimension of the circular waveguide is chosen so that the circular waveguide  $TE_{11}$  mode can propagate (since the field distribution of this mode forms a most natural transition between rectangular waveguide  $TE_{11}$  mode and corrugated waveguide  $HE_{11}$  mode), whereas most of the other modes are either cut off by the circular waveguide dimensions or cannot be excited due to the symmetry of the waveguide.

The cutoff wavelengths for the circular waveguide  $TE_{ni}$  and  $TM_{ni}$  modes have the following expressions.

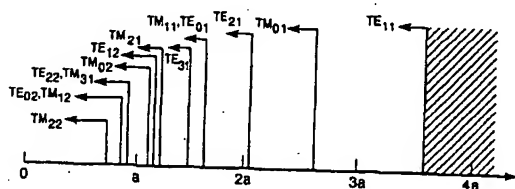


Fig. 17. Circular waveguide modes and their cutoff wavelengths.

TM modes:

$$(\lambda_c)_{TM_{ni}} = \frac{2\pi a}{\mu_{ni}} \quad (A2)$$

where  $\mu_{ni}$  is the  $i$ th root of  $n$ th-order Bessel function, and

TE modes:

$$(\lambda_c)_{TE_{ni}} = \frac{2\pi a}{\nu_{ni}} \quad (A3)$$

where  $\nu_{ni}$  is the  $i$ th root of the first derivative of the  $n$ th-order Bessel function.

Using these formulas, the cutoff wavelengths can be calculated, and they are plotted in Fig. 17. Our operation range of 70–115 GHz corresponding to  $\lambda$  in the range of 4.28–2.6 mm. With a choice of circular waveguide radius  $a = 0.061$  in = 1.55 mm, the corresponding  $\lambda$  will be in the range of  $1.68a$  and  $2.77a$ . In this region, the only propagating modes are  $TE_{11}$ ,  $TM_{01}$ , and  $TE_{21}$ . Among them, the first one is the desired working mode, and the second and third have the field symmetries which do not couple energy from rectangular  $TE_{11}$  mode. This choice of  $a$  is mainly to cut off the most harmful  $TM_{11}$  mode, while still keeping the size of the circular waveguide large enough to reduce metal loss.

The final choice of the dimensions for the rectangular-to-circular waveguide transition section is shown in Fig. 12. Small sections of rectangular and circular waveguide attached at each end of the transition section are for the purposes of securing both the smooth transition and the higher order mode cutoff.

## REFERENCES

- [1] X. Zhang, "Design and measurement of conical corrugated feed horns for the BIMA array," *Berkeley-Illinois-Maryland Array Memo. Ser.*, no. 17, 1991.
- [2] G. L. James, "Analysis and design of  $TE_{11}$ -to- $HE_{11}$  corrugated cylindrical waveguide mode converters," *IEEE Trans. Microwave Theory Tech.*, vol. MTT-29, pp. 1059–1066, 1981.
- [3] —, "TE<sub>11</sub> to TM<sub>11</sub> cylindrical waveguide mode converters using ring-loaded slots," *IEEE Trans. Microwave Theory Tech.*, vol. MTT-30, pp. 278–285, 1982.
- [4] R. Padman, J. A. Murphy, and R. E. Hills, "Gaussian mode analysis of Cassegrain antenna efficiency," *IEEE Trans. Antennas. Propagat.*, vol. AP-35, pp. 1093–1103, 1987.
- [5] P. J. B. Clarricoats and A. D. Oliver, *Corrugated Horns for Microwave Antennas*. London: Peter Peregrinus, 1984.
- [6] B. MacA. Thomas, "Theoretical performance of prime-focus paraboloids using cylindrical hybrid-mode feeds," *Proc. IEE*, vol. 118, pp. 75–85, 1971.
- [7] C. Dragone, "Reflection, transmission, and mode conversion in a corrugated feed," *Bell Syst. Tech. J.*, pp. 835–867, July–Aug. 1977.
- [8] —, "Characteristics of a broadband microwave corrugated feed: A comparison between theory and experiment," *Bell Syst. Tech. J.*, pp. 869–888, July–Aug. 1977.
- [9] P. F. Goldsmith, "Quasi-optical techniques at millimeter and submillimeter wavelengths," in *Infrared and Millimeter Waves*, vol. 6, 1982, ch. 5.
- [10] D. Hoppe, "CWGSCAT", a program package developed at JPL, distributed by COSMIC Co.



Xiaolei Zhang (S'88) received the B.E. degree from Tsinghua University, Beijing, China, in July 1985, and the M.S. and Ph.D. degrees from the University of California at Berkeley, in December 1987 and December 1992, respectively, all in the field of electrical engineering and computer sciences.

Her Ph.D. dissertation work included microwave and optical instrumentation with the Berkeley-Illinois-Maryland millimeter interferometer, as well as radio astronomical observation and theoretical studies of the galactic dynamics problems. She is currently a Smithsonian Postdoctoral Fellow at the Harvard-Smithsonian Center for Astrophysics, working on holography and feed design for the submillimeter array project, and on astronomical research.